Communication

Dual-CP Antenna With Wide-HPBW and Wide-ARBW Performance for Wide-Angle Scanning Phased Array

Liang-Xin Xia, Neng-Wu Liu, Lei Zhu, and Guang Fu

***Abstract*— In this communication, a novel dual-circularly polarized (CP) antenna with both wide half-power beamwidth (HPBW) and wide axial-ratio beamwidth (ARBW) is proposed. Based on the septum circular polarizer, the principle about HPBW improvement of its $|E_\theta|$ and $|E_\varphi|$ components is extensively studied. It proves that the metal rings around the top surface could be used to enhance the low elevation gain and extend its HPBW of $|E_\theta|$ components. Subsequently, a set of slots is introduced on the waveguide to expand the HPBW of its $|E\varphi|$ component. With these arrangements, both ARBW and HPBW parameters of the antenna are simultaneously widened while keeping wide impedance bandwidth as desired. In addition, the antenna element is constructed as the 1 × 8 phased array for wide-angle scanning in such a way that the array antenna can satisfactorily achieve a wide CP scanning range and stable radiation pattern. Finally, the proposed antenna is designed, fabricated, and measured. The results evidently reveal that the proposed element can simultaneously achieve 3-dB HPBW and 3-dB ARBW in the range of 130° in 3.8–4.2 GHz, and its inspired array can effectively achieve beam scanning from -60° to 60° in 3.9–4.2 GHz.**

***Index Terms*— Dual-circularly polarization, metal rings, phased array, slots, wide axial-ratio beamwidth (ARBW), wide half-power beamwidth (HPBW), wide-angle scanning.**

I. Introduction

In satellite communications, circularly polarized (CP) antennas with wide half-power beamwidth (HPBW) and axial-ratio beamwidth (ARBW) are highly demanded due to their several unique advantages, such as anti-interference and polarization distortion elimination. Unfortunately, the traditional CP antennas [1], [2], [3], [4] always suffer from either narrow HPBW or narrow ARBW, especially in a wide working band, thus restricting their application in satellite communications. To improve the HPBW, various methods have been proposed over the past two decades. First, the cavity-backed ground could significantly improve the HPBW to 150° [5]. Second, for microstrip antennas, the choice of dielectric material may affect its performance, with larger substrates resulting in a wide HPBW of around 130° [6], [7]. However, these methods may not be suitable for wide-angle scanning phased arrays due to surface wave and space limitations. Third, loading parasitic elements around the core radiator has been shown to improve HPBW. Vertical currents in [8] and [9] enhance radiation gain at low elevation, expanding HPBW to above 114°. Meanwhile, in [10], parasitic units on top layer also expanded the HPBW to 140°, but its bandwidth is very narrow. In an array environment, ring-slot elements can also achieve a wide HPBW. However, their AR bandwidth is limited by the excitation method [11]. In addition, metal rings added to the waveguide's outer wall in [12] achieve a wide HPBW of about 127° but may suffer from narrow ARBW or large lateral size.

Apart from the wide HPBW, the ARBW of the antenna is also important for the quality of communication over a wide angle. Several distinctive techniques have been proposed so far. The first technique was to reshape the ground plane as the metal walls [13] so as to extend its ARBW of above 165°. The second technique was to adjust the phase of $|E_\theta|$ and $|E_\varphi|$ by loading special structures, which could be employed for ARBW enhancement of above 180° [14], [15]. In the third technique, the ARBW was effectively improved by introducing additional vertical currents around the primary patch [16] and dipoles [17]. In the fourth technique, changing the radiation structure without adding parasitic elements, such as forming a tapered elliptical cavity inside or above the dielectric plate in [18] and [19], achieves a wide ARBW of about 121°. Finally, adjusting the aperture of radiation [20], [21], [22] or stacked patches [23] can achieve a wider ARBW. By adjusting the array size of a 2 × 2 electric dipole or magnetic dipole, the antenna's ARBW can exceed 126°, but this requires a more complex feeding network. However, these antennas mentioned above tend to keep narrow HPBW, large lateral dimensions, or narrow bandwidth.

From the above discussion, it can be well understood that few antennas can maintain a wide HPBW and ARBW simultaneously, especially in the wide operating band. In phased scanning arrays, the beamwidth of the element often determines the maximum scan angle of the array, and narrow HPBW and ARBW units can only achieve small beam scanning [24]. Meanwhile, CP scanning arrays generally require a low AR during scanning [25]. In [26] and [27], a lower AR could be achieved for large-angle scanning, but the narrow HPBW of the antenna unit results in a higher gain attenuation of 5 dB for array scanning. To further improve the performance of array scanning, the HPBW and ARBW of the array unit are often required to be wide enough. The antenna in [28] and [29] has been improved to widen the beam and achieve scanning ability in the range of ±40° and ±49°, respectively. When the ARBW and HPBW of the antenna unit are both greater than 120°, the array can achieve gain attenuation and axial ratio within 3 dB when scanning at an angle of about 60°, but the operating bandwidth is kept as small as below 5% [30], [31].

In this communication, we propose and develop a dual-CP antenna with wide HPBW and wide ARBW as illustrated in Fig. 1. This antenna consists of the septum circular polarizer, metal ring, and waveguide wall with grooving. Noticing that, by adjusting the position and size of the metal ring and vertical slot, the $|E_\theta|$ and $|E_\varphi|$ components of the antenna are both increased in Fig. 1. The remainder of this work is organized as follows. Section II illustrates the working principle about how to realize the wide-HPBW and wide-ARBW for the CP element. In Section III, the wide-angle phase

Manuscript received 23 October 2023; revised 1 February 2024; accepted 20 February 2024. Date of publication 13 March 2024; date of current version 7 May 2024. This work was supported in part by the National Natural Science Foundation of China through the General Program under Grant 62271364 and in part by the Key Research and Development Program of Shaanxi Program under Grant 2023-GHZD-45. *(Corresponding author: Neng-Wu Liu.)*

Liang-Xin Xia, Neng-Wu Liu, and Guang Fu are with the National Key Laboratory of Antennas and Microwave Technology, Xidian University, Xi'an 710071, China (e-mail: yb47448@umac.mo; nwliu@xidian.edu.cn).

Lei Zhu is with the Department of Electrical and Computer Engineering, Faculty of Science and Technology, University of Macau, Macau, SAR, China.

Color versions of one or more figures in this communication are available at https://doi.org/10.1109/TAP.2024.3373064.

Digital Object Identifier 10.1109/TAP.2024.3373064

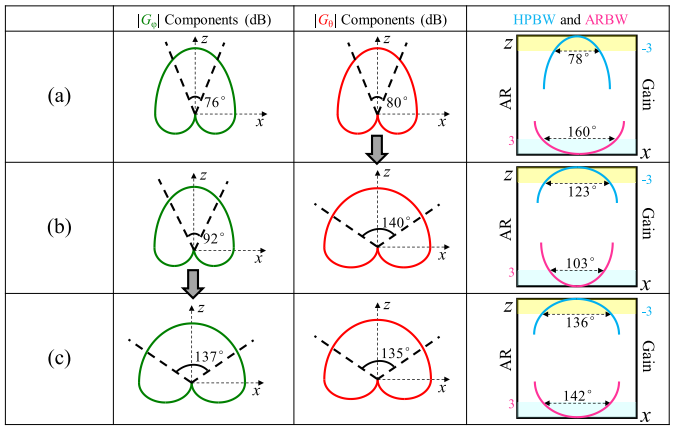

Fig. 1. Variation in radiation patterns of three distinctive antennas for HPBW and ARBW enhancement. (a) Traditional CP antenna (Antenna 1). (b) CP antenna with ring (Antenna 2). (c) CP antenna with ring and slot (Antenna 3).

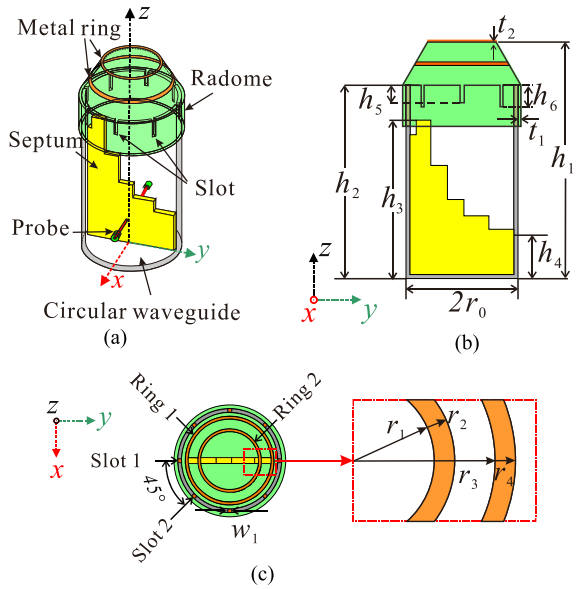

Fig. 2. Configuration of the proposed wide beam antenna. (a) Three-dimensional view. (b) Side view. (c) Dielectric radome.

array based on the above element is extensively investigated. Finally, we present our conclusion in Section IV.

II. Dual-CP Wide-Beam Antenna Element

In this section, the working principle about how to achieve both of wide HPBW and wide ARBW of the CP antenna element will be extensively investigated.

A. Antenna Configuration

Fig. 2 shows the configuration of the proposed element with wide HPBW and wide ARBW simultaneously. It consists of a septum circular waveguide, dielectric radome, metal rings, and feeding coaxial cables. In order to gain the dual-CP polarized performance, a metal stepped septum is loaded inside the circular waveguide [32], [34]. Besides, a dielectric radome ($\varepsilon_r = 2.75$ and $\tan(\delta) = 0.0253$) with the printed metal ring is introduced on the top surface of the circular waveguide in Fig. 2(c), aiming to widen its $|E_\theta|$ component and HPBW. In addition, a set of linear slots is cut on the circular waveguide in order to widen its $|E_\varphi|$ component and ARBW. The simulation and optimization of the antenna are carried out using the FEM of Ansys HFSS 2021 version software, and the optimized antenna parameters are tabulated in Table I.

TABLE I
Optimized Parameters of the Proposed Antenna

Parameters	h_1	h_2	h_3	h_4	h_5	h_6	t_1
Values (mm)	117	96	79	21	8.5	10.5	1.5
Parameters	t_2	r_0	r_1	r_2	r_3	r_4	w_1
Values (mm)	1	54	15.5	16.5	22	23	2

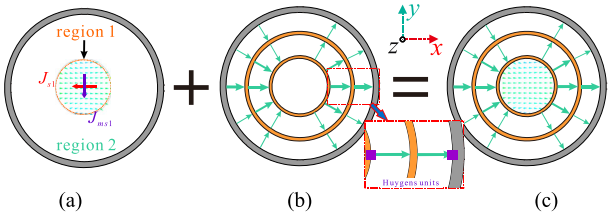

Fig. 3. Distributions of instant electric fields for Antenna 2. (a) Electric field (E_1) within the rings (region 1). (b) Electric field (E_2) between two metal rings (region 2). (c) EMCs and ECs of the waveguide loaded with two metal rings (Antenna 2).

B. Working Principle of $|E_\theta|$ and $|E_\varphi|$ Beamwidth Improvement

Next, let us elaborate on the working principles behind the enhancement of the $|E_\theta|$ and $|E_\varphi|$ components, based on the antenna evolution process depicted in Fig. 1.

1) Traditional CP Antenna (Antenna 1): As is well known, for the traditional waveguide (Antenna 1), the HPBW of $|E_\theta|$ and $|E_\varphi|$ components is kept as small as around 80° as shown in Fig. 1(a), thus restricting its application for the phased array. To tackle this issue, we investigate the theoretical working principle for increasing the HPBW of $|E_\theta|$ and $|E_\varphi|$ components. Due to the electric-field distribution at the small aperture waveguide being approximately uniform, the amplitude of the electric field at the waveguide interface is assumed to be equal and set to E_1 to simplify the subsequent calculation. In [35], the radiation patterns of the traditional linearly polarized (LP) waveguide antenna could be calculated by using the equivalent magnetic currents (EMCs) and equivalent currents (ECs), which is expressed as follows:

$$\mathrm{E_{-plane}}: \overrightarrow{E_\theta} = j\frac{\pi\rho^2 E_1}{2\lambda r}(1+\cos\theta)\frac{2J_1(\beta\rho\sin\theta)}{\beta\rho\sin\theta}e^{-j\beta r}\widehat{\theta} \quad (1)$$

$$\mathrm{H_{-plane}}: \overrightarrow{E_\varphi} = j\frac{\pi\rho^2 E_1}{2\lambda r}(1+\cos\theta)\frac{2J_1(\beta\rho\sin\theta)}{\beta\rho\sin\theta}e^{-j\beta r}\widehat{\varphi} \quad (2)$$

where ρ represents the inner radius of the waveguide.

2) CP Antenna With Ring (Antenna 2):

a) $|E_\theta|$ component: Initially, the metal rings are loaded on the top surface of the waveguide to extend the HPBW of its $|E_\theta|$ component, and the relevant electric-field distributions are presented in Fig. 3. Herein, the ring-loaded antenna radiation field mainly consists of two parts: 1) electric field within the radius r_1 of the circular waveguide in Fig. 3(a) and 2) electric field between the metal rings in Fig. 3(b). The normalized radiation pattern generated by region 1, expressed as $E_{\theta 1} = E_\theta$ ($\rho = r_1 = 15.5$ mm), is depicted in Fig. 4(a). It is observed that the HPBW of the $|E_\theta|$ component increases as ρ decreases.

In fact, the radiated field in region 2 is mainly generated by the field between rings. For the sake of analysis, the field of region 2 is regarded as a nonplanar array composed of four Huygens elements as shown in Fig. 5(b) and (c), so the radiation pattern in $\varphi = 0°$ can be calculated as follows:

$$\overrightarrow{E_{\theta 21}} = j\frac{E_2 dxdy}{2\lambda r}(1+\cos(\theta+\theta_0)) \times \cos\left(\frac{1}{2}kd_2\sin(\theta+\theta_0)\right)\cdot e^{-j\beta r}\widehat{\theta} \quad (3)$$

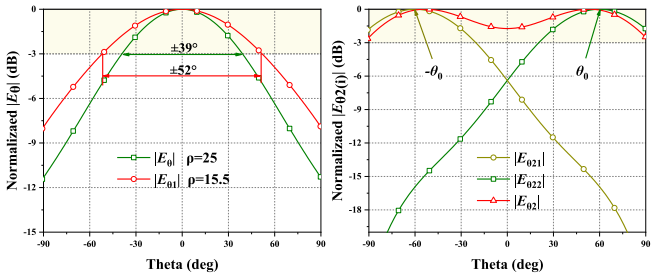

Fig. 4. Normalized patterns obtained by theoretical calculation at 4 GHz, $\varphi = 0°$. (a) Antenna 1 and region 1 in Antenna 2. (b) Region 2 in Antenna 2.

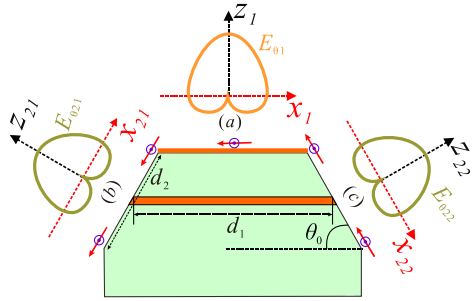

Fig. 5. Radiation patterns of each region in Antenna 2. (a) Region 1. (b) Region 21. (c) Region 22.

$$\overrightarrow{E_{\theta 22}} = j\frac{E_2 dxdy}{2\lambda r}\left(1+\cos\left(\theta-\theta_0\right)\right) \times \cos\left(\frac{1}{2}kd_2\sin\left(\theta-\theta_0\right)\right)\cdot e^{-j\beta r}\widehat{\theta}. \tag{4}$$

Then, the far-field radiation for region 2 is as follows:

$$\overrightarrow{E_{\theta 2}} = \left|\overrightarrow{E_{\theta 21}}\right| + \left|\overrightarrow{E_{\theta 21}}\right| e^{jkd_1\sin\theta}\widehat{\theta}. \tag{5}$$

The normalized patterns of (3)–(5) are plotted in Fig. 4(b). It can be seen that the far-field radiation of region 2 approximates the "saddle" shape. Because the actual field of region 2 is distributed on a cross section, the actual pattern's sag is deeper than that shown in Fig. 4(b). Meanwhile, Fig. 6 indicates the superposition of the far-field pattern in regions 1 and 2 of Antenna 2. It is evident that the HPBW of the $|E_\theta|$ component greatly increases because of the ring loading.

b) $|E_\varphi|$ component: For $|E_\varphi|$ component, it can also be composed of two parts: the radiation of regions 1 and 2, namely, the $|E_\varphi|$ component generated by rotating the field along the center by 90°, as shown in Fig. 3. For a field uniformly distributed in a circular region, the far-field patterns are basically the same in $\varphi = 0°$ and $\varphi = 90°$. As seen in Fig. 4(a), compared to Antenna 1, the HPBW formed in region 1 is wider at ±52°. Therefore, the radiation beam formed by region 2 is narrower than that of Antenna 1 as a whole. Due to the fact that only the horizontal field component in the ring region of Antenna 2 generates the $|E_\varphi|$ component, the far-field contribution of region 2 is reduced when being superimposed. Finally, the HPBW of the $|E_\varphi|$ component of Antenna 2 is kept between 78° and 104°.

c) HPBW and ARBW: With the above arrangements, the CP antenna can be regarded as the superposition of the antenna as shown in Fig. 3 and the orthogonal one with a phase difference of 90°, so as to obtain the $|E_\theta|$ and $|E_\varphi|$ components of the resultant CP antenna. As such, the AR performance as a function of angle θ is derived as

$$AR\left(\theta\right) = \left|E_\theta\left(\theta\right)/E_\varphi\left(\theta\right)\right|. \tag{6}$$

As a result, the HPBW of the $|E_\theta|$ and $|E_\varphi|$ components of Antenna 2 is both increased, but the extent of the increase of the $|E_\theta|$ component is much greater than that of $|E_\varphi|$, so the HPBW of Antenna 2 becomes wider and the ARBW becomes narrower, as shown in Fig. 1(b).

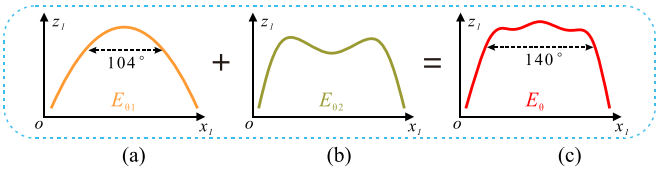

Fig. 6. Radiation pattern comparison for Antenna 2 under different regions at 4 GHz, $\varphi = 0°$. (a) Region 1 in Antenna 2. (b) Region 2 in Antenna 2. (c) Antenna 2.

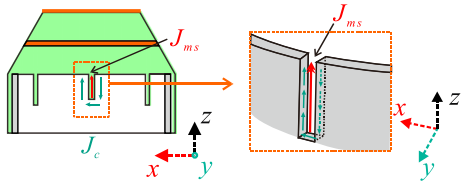

Fig. 7. Distributions of simulated currents near the vertical slot for the antenna loaded with rings and slots (Antenna 3).

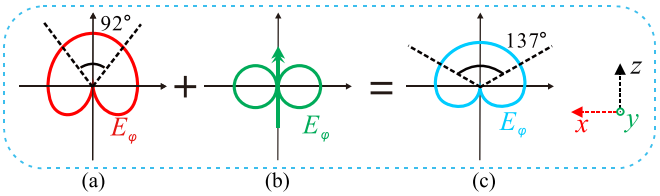

Fig. 8. Vertical radiation patterns for different antennas. (a) Antenna 2. (b) Vertical magnetic current. (c) Antenna 3.

C. CP Antenna With Ring and Slot (Antenna 3)

The introduction of rings can widen the HPBW of the antenna's $|E_\theta|$ component, as discussed above. Unfortunately, the $|E_\varphi|$ radiated field of the antenna only increases slightly, resulting in reducing the ARBW of the antenna. In order to address this issue, our next main target is to investigate the working principle about how to increase the HPBW of its $|E_\varphi|$ component.

As is well known, the vertical magnetic currents could be introduced for the HPBW extension of the $|E_\varphi|$ components. As such, a set of linear slots were etched out on the side edges of the circular waveguide to construct a new radiation source by cutting the currents on the inner wall through the grooves, as shown in Fig. 7. Herein, the radiated fields from these slots could be calculated by using the vertical magnetic current ($J_{\rm ms}$). The evolution process of the far-zone radiation patterns is presented in Fig. 8 to illustrate this working principle. It can be seen herein that Antenna 2 generates the narrow HPBW of $|E_\varphi|$ component (92°) and low radiation gain around the low elevation angles in Fig. 8(a). By contrast, the vertical slots contribute to the peak $|E_\varphi|$ radiated fields in the horizontal plane in Fig. 8(b). Therefore, combining these two radiation fields together can significantly increase the radiation gain of the $|E_\varphi|$ component at low elevation angles [10]. According to (6), it is evident that when the magnitudes of the $|E_\theta|$ and $|E_\varphi|$ components are approximately equal, the antenna's 3-dB ARBW is improved, as shown in Fig. 1(c).

D. Comparison of the Beamwidths for Antennas 1–3

To better illustrate the performance variations caused by structural differences, Fig. 9 depicts the HPBW and 3-dB ARBW of Antennas 1–3 varying with frequency. The observed variations in HPBW and ARBW over the operating band align with the aforementioned working principles. Until now, the working principle about how to achieve wide CP beamwidth (ARBW and HPBW) of the antenna

TABLE II
PERFORMANCE COMPARISON OF THE ANTENNA ELEMENTS

Ref.	Imped-BW	No. of pol.	Volume(λ_c^{-3})	ARBW(3dB)	HPBW	AR-BW	Pattern-BW
[4]	19%	2	0.15	110°↓	60°↓	16%	NG
[9]	10%↓	1↓	0.70↓	120°↓	110°↓	10%↓	7%↓
[11]	30%	1↓	0.20	100°↓	120°↓	4%↓	NG
[18]	13%↓	1↓	0.011	121°↓	102°↓	3.5%↓	3.2%↓
[19]	11%↓	1	1.30↓	134°	60°↓	11%↓	NG
[23]	13%	1↓	0.30	120°↓	100°↓	13%↓	13%
This work	**19%**	**2**	**0.61**	**≥130°**	**≥130°**	**16.8%**	**10%**

Pattern-BW represents the pattern bandwidth that meets the ARBW and HPBW

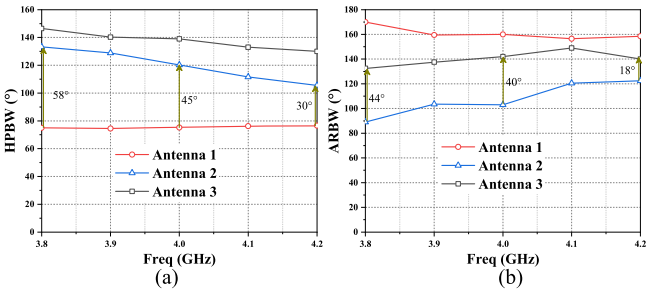

Fig. 9. (a) HPBW and (b) 3-dB ARBW of Antennas 1–3 varying with frequency.

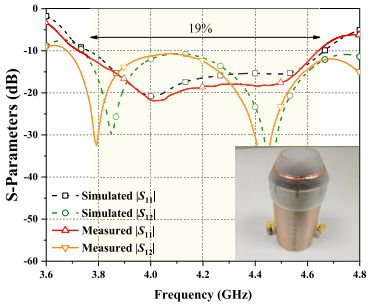

Fig. 10. Simulated and measured results of $|S_{11}|$ and $|S_{12}|$ for the proposed antenna.

has been deeply investigated, and it could be well applied for the wide-angle scanning phased array in the following.

E. Fabrication and Performance Validation

In order to verify the above working principle, the antenna has been fabricated and measured. Fig. 10 gives the comparison between simulated and measured S-parameters, which shows that the antenna exhibits good impedance matching within the operating band and achieves a radiation efficiency of over 90%. Although its worst isolation is 11 dB, it can be improved to over 20 dB through the additional decoupling network. Figs. 11 and 12 illustrate the simulated and measured LHCP patterns for the wide-beam antenna, showcasing a wide 3-dB beamwidth in both the *xz* and *yz* planes. Most importantly, the antenna has successfully achieved 3-dB gain reduction and low axial ratio simultaneously in the range of 130°.

Fig. 13 shows the simulated and measured results of the antenna gain and axial-ratio variations with frequency. The simulated results generally align with the measured ones, indicating a stable pattern within the 3.8–4.2-GHz frequency range. Compared with other existing wide-beam antennas referred in the literature, the dual-polarized CP antenna proposed in this work has its own attractive advantages in terms of maximum 3-dB ARBW, HPBW, and number of polarization states, as shown in Table II. Despite its feeding structure resulting in a higher profile height, the antenna is ideal for wide-angle scanning

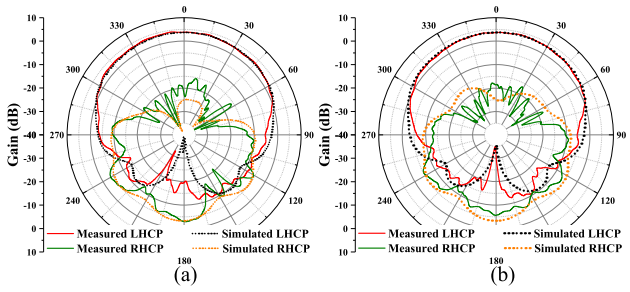

Fig. 11. Simulated and measured radiation patterns for the proposed antenna when port 1 is excited at 4 GHz. (a) *xz* plane. (b) *yz* plane.

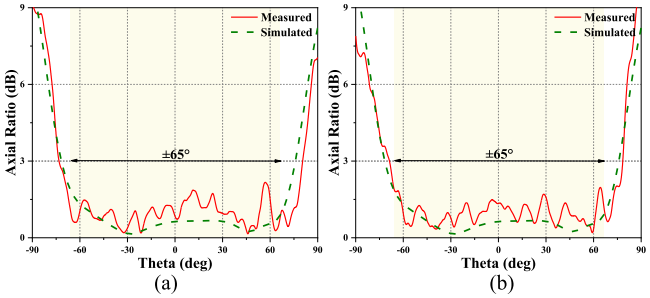

Fig. 12. Simulated and measured AR beam for the proposed antenna when port 1 is excited at 4 GHz. (a) *xz* plane. (b) *yz* plane.

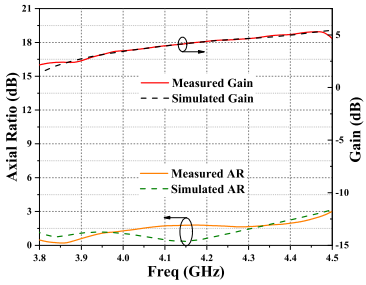

Fig. 13. Simulated and measured results of Gain and AR versus frequency when port 1 is excited.

TABLE III
OPTIMIZED PARAMETERS OF THE PHASED ARRAY ANTENNA

Parameters	d_0	d_1	w_0	l_0	h_0
Values (mm)	64	60	150	300	39

array antennas used in exploration, as it has a wide HPBW and ARBW of over 130° within a 10% frequency range.

III. DUAL-CP WIDE-ANGLE SCANNING PHASED ARRAY

On the basis of the above CP element, the phased array antenna is finally designed and fabricated with its photograph in Fig. 14. Herein, the array antenna consists of eight antenna elements with wide beams

TABLE IV

PERFORMANCE COMPARISON BETWEEN THE PROPOSED AND THESE PREVIOUS ARRAY ANTENNAS

Ref.	[25]	[26]	[27]	[30]	[31]	**This work**
Pattern-BW	10%	13.3%	1.8%↓	2%↓	< 5%↓	**(3.9-4.2)7.4%**
No. of pol.	1↓	2	1↓	1↓	2	**2**
Height (×λ_c)	0.1	1.23	0.16	0.1	0.065	**0.8**
Scanning angle (AR<4dB,△G<3dB)	-50°~50°↓	-38°~38°↓	-45°~45°↓	-66°~66°	-59°~58°	**-60°~60°**

Pattern-BW represents the pattern bandwidth that meets the scanning angle limitation
△G represents the gain attenuation value

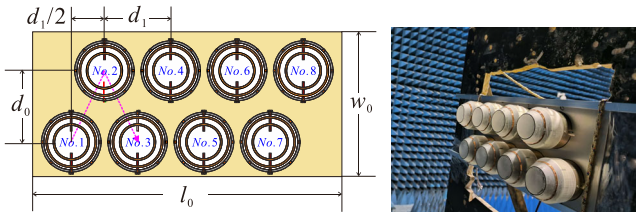

Fig. 14. Configuration and photographs of the proposed array.

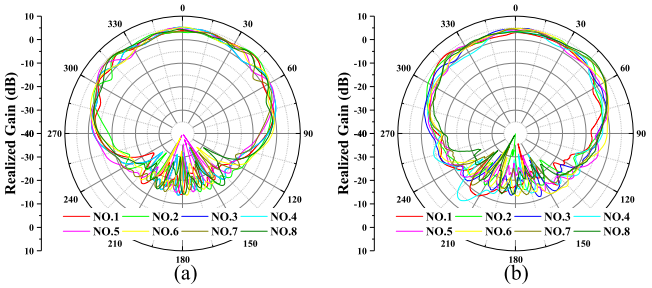

Fig. 15. Simulated and measured active patterns of the eight cells in the *yz* plane at 4 GHz (LHCP). (a) Simulated. (b) Measured.

arranged in a triangular grid, and these units are equally arranged and fixed by metal plates. The metal plate is h_0 away from the waveguide aperture. According to the results of experimental simulation, all of the optimized parameters of the array are listed in Table III.

A. Results of Active Patterns of Elements

In order to simplify the measurement procedure and setup, the scanning characteristics of the array are obtained by measuring the active patterns of the array units first and then synthesizing them without using the phase shifter. Here, the active pattern stands for the pattern obtained by feeding a unit and all other units are connected to the matching load. Fig. 15 shows the active patterns of the array units for simulation and measurement. It can be found that the elements in the array still have a wide beamwidth and the simulated results are basically consistent with the measured results.

B. Performance of Phased Array

Kelley and Stutzman [36] introduced the method of obtaining the scanning characteristics of the phased array from the active patterns of the units. Since the active patterns of the units contain the coupling effect between the unit and the surrounding unit or the environment, the scanning beam of the phased array can be obtained by adding the equal phase difference a to the active patterns. The following equation indicates the formula of the array mode synthesis as given in [36]:

$$E_{\text{array}} = \sum_{m=1}^{M} E_{\text{m}}(\theta,\varphi)\, e^{jma} e^{-jk_0 m \frac{d_1}{2}\sin(\theta)\sin(\varphi)}. \quad (7)$$

The actual array scanning pattern E_{array} can be obtained by (7), where $E_{\text{m}}(\theta,\varphi)$ is the active pattern of the mth element. The second

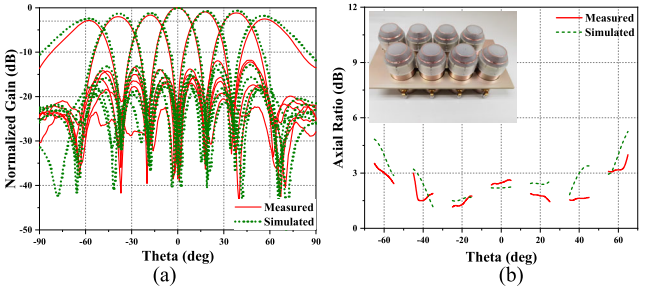

Fig. 16. Measured and simulated results in the *yz* plane at 4 GHz (LHCP). (a) Normalized patterns of different scanning angles. (b) AR pattern.

term is the phase given by the mth element. The remaining two parts are the phases assigned to the mth unit and the spatial phase difference caused by the unit space in different directions. Hence, the measured active patterns of the array units are synthesized using (7) to generate radiation patterns of the array at 0°, ±20°, ±40°, and ±60°, as depicted in Fig. 16. As a result, the proposed array has a gain reduction of less than 3 dB and an axial ratio of less than 4 dB in the ±60° scanning range. The array antenna indeed exhibits good CP wide-angle scanning characteristics.

Finally, a comparison between our work and previous works is provided in Table IV. In [25] and [27], the proposed antenna can maintain low AR at a large angle, but the gain reduction is large and only single polarization. The antenna in [30] can achieve less than 3-dB AR and 3-dB gain reduction in the scan range of ±66°, but it can only achieve circular polarization in one plane and has a narrow bandwidth. The septum circular polarizer proposed in [26] is designed for 5G communication but is limited by its narrow beam. In contrast, our proposed antenna can effectively address this issue by offering low AR and high gain within the ±60° range.

IV. CONCLUSION

In this communication, a dual-CP antenna with wide HPBW and wide ARBW has been proposed and designed. First, by loading a metal ring on the antenna aperture, the HPBW of its $|E_\theta|$ components is successfully widened. Second, by introducing the slots on the waveguide, the HPBW of its $|E_\varphi|$ components is further increased. With these arrangements, the proposed element is fabricated and measured, which reveals that the antenna has achieved 3-dB gain reduction and low axial ratio simultaneously in the range of 130° operating in 3.8–4.2 GHz. Finally, a 1 × 8 eight-element linear array is constructed based on the above element. Good agreement between simulation and measurement has demonstrated that the array has a wide scanning angle of ±60°.

REFERENCES

[1] A. Khidre, F. Yang, and A. Z. Elsherbeni, "Circularly polarized beam-scanning microstrip antenna using a reconfigurable parasitic patch of tunable electrical size," *IEEE Trans. Antennas Propag.*, vol. 63, no. 7, pp. 2858–2866, Jul. 2015.

[2] M.-C. Tang, X. Chen, M. Li, and R. W. Ziolkowski, "A bandwidth-enhanced, compact, single-feed, low-profile, multilayered, circularly polarized patch antenna," *IEEE Antennas Wireless Propag. Lett.*, vol. 16, pp. 2258–2261, 2017.

[3] L. Lu, Y.-C. Jiao, H. Zhang, R. Wang, and T. Li, "Wideband circularly polarized antenna with stair-shaped dielectric resonator and open-ended slot ground," *IEEE Antennas Wireless Propag. Lett.*, vol. 15, pp. 1755–1758, 2016.

[4] C. Zhang, X. Liang, X. Bai, J. Geng, and R. Jin, "A broadband dual circularly polarized patch antenna with wide beamwidth," *IEEE Antennas Wireless Propag. Lett.*, vol. 13, pp. 1457–1460, 2014.

[5] Y. Sun, K. W. Leung, and K. Lu, "Broadbeam cross-dipole antenna for GPS applications," *IEEE Trans. Antennas Propag.*, vol. 65, no. 10, pp. 5605–5610, Oct. 2017.

[6] K. Y. Lam, K.-M. Luk, K. F. Lee, H. Wong, and K. B. Ng, "Small circularly polarized U-slot wideband patch antenna," *IEEE Antennas Wireless Propag. Lett.*, vol. 10, pp. 87–90, 2011.

[7] X. L. Bao and M. J. Ammann, "Dual-frequency dual circularly-polarised patch antenna with wide beamwidth," *Electron. Lett.*, vol. 44, no. 21, pp. 1233–1234, Oct. 2008.

[8] H. J. Sun, L. Shi, and J. T. Li, "A compact broadband circularly polarized composite antenna with wide beamwidth," *Microw. Opt. Technol. Lett.*, vol. 50, no. 11, pp. 2973–2975, Nov. 2008.

[9] L. Wang, H.-C. Yang, and Y. Li, "Design of a new printed dipole antenna using in high latitudes for Inmarsat," *IEEE Antennas Wireless Propag. Lett.*, vol. 10, pp. 358–360, 2011.

[10] Z.-K. Pan, W.-X. Lin, and Q.-X. Chu, "Compact wide-beam circularly-polarized microstrip antenna with a parasitic ring for CNSS application," *IEEE Trans. Antennas Propag.*, vol. 62, no. 5, pp. 2847–2850, May 2014.

[11] A. K. Bhattacharyya, A. R. Cherrette, and R. D. Bruno, "Analysis of ring-slot array antenna using hybrid matrix formulation," *IEEE Trans. Antennas Propag.*, vol. 61, no. 4, pp. 1642–1650, Apr. 2013.

[12] B.-B. Huang, N.-W. Liu, G. Fu, and L.-X. Xia, "A dual-circularly polarized antenna with wide-beamwidth," in *IEEE MTT-S Int. Microw. Symp. Dig.*, Chongqing, China, Nov. 2021, pp. 22–24.

[13] S. X. Ta and I. Park, "Crossed dipole loaded with magneto-electric dipole for wideband and wide-beam circularly polarized radiation," *IEEE Antennas Wireless Propag. Lett.*, vol. 14, pp. 358–361, 2015.

[14] Y. Nasimuddin, S. Anjani, and A. Alphones, "A wide-beam circularly polarized asymmetric-microstrip antenna," *IEEE Trans. Antennas Propag.*, vol. 63, no. 8, pp. 3764–3768, Aug. 2015.

[15] Z. Wang, S. Liu, and Y. Dong, "Electrically small, low-Q, wide beam-width, circularly polarized, hybrid magnetic dipole antenna for RFID application," *IEEE Trans. Antennas Propag.*, vol. 69, no. 10, pp. 6284–6293, Oct. 2021.

[16] X. Chen, L. Yang, J.-Y. Zhao, and G. Fu, "High-efficiency compact circularly polarized microstrip antenna with wide beamwidth for airborne communication," *IEEE Antennas Wireless Propag. Lett.*, vol. 15, pp. 1518–1521, 2016.

[17] W. J. Yang, Y. M. Pan, and S. Y. Zheng, "A low-profile wideband circularly polarized crossed-dipole antenna with wide axial-ratio and gain beamwidths," *IEEE Trans. Antennas Propag.*, vol. 66, no. 7, pp. 3346–3353, Jul. 2018.

[18] K.-B. Ng, C. H. Chan, and K.-M. Luk, "Low-cost vertical patch antenna with wide axial-ratio beamwidth for handheld satellite communications terminals," *IEEE Trans. Antennas Propag.*, vol. 63, no. 4, pp. 1417–1424, Apr. 2015.

[19] X. Bai, S.-W. Qu, S. Yang, J. Hu, and Z.-P. Nie, "Millimeter-wave circularly polarized tapered-elliptical cavity antenna with wide axial-ratio beamwidth," *IEEE Trans. Antennas Propag.*, vol. 64, no. 2, pp. 811–814, Feb. 2016.

[20] L. Zhu and N. Liu, "Multimode resonator technique in antennas: A review," *Electromagn. Sci.*, vol. 1, no. 1, pp. 1–17, Mar. 2023.

[21] Y. Luo, Q.-X. Chu, and L. Zhu, "A low-profile wide-beamwidth circularly-polarized antenna via two pairs of parallel dipoles in a square contour," *IEEE Trans. Antennas Propag.*, vol. 63, no. 3, pp. 931–936, Mar. 2015.

[22] X. Zhang, L. Zhu, and N.-W. Liu, "Pin-loaded circularly-polarized patch antennas with wide 3-dB axial ratio beamwidth," *IEEE Trans. Antennas Propag.*, vol. 65, no. 2, pp. 521–528, Feb. 2017.

[23] M. Koubeissi et al., "WideBand WideAngle circular polarization of a multilayer patch antenna," in *Proc. 4th Eur. Conf. Antennas Propag.*, Barcelona, Spain, Apr. 2010, pp. 1–4.

[24] F. Zhang, G.-M. Yang, Y.-Q. Jin, F. Peng, and J. Mo, "Space-borne deployable P-band dual-circular-polarization flexible antenna array," *IEEE Antennas Wireless Propag. Lett.*, vol. 16, pp. 2529–2533, 2017.

[25] J.-W. Kim, S.-C. Chae, H.-W. Jo, T.-D. Yeo, and J.-W. Yu, "Wideband circularly polarized phased array antenna system for wide axial ratio scanning," *IEEE Trans. Antennas Propag.*, vol. 70, no. 2, pp. 1523–1528, Feb. 2022.

[26] Q. Wu, J. Hirokawa, J. Yin, C. Yu, H. Wang, and W. Hong, "Millimeter-wave multibeam endfire dual-circularly polarized antenna array for 5G wireless applications," *IEEE Trans. Antennas Propag.*, vol. 66, no. 9, pp. 4930–4935, Sep. 2018.

[27] Y. Yang, Y. Ban, Q. Yang, J. Lian, Q. Sun, and G. Wu, "Millimeter wave wide-angle scanning circularly polarized antenna array with a novel polarizer," *IEEE Trans. Antennas Propag.*, vol. 70, no. 2, pp. 1077–1086, Feb. 2022.

[28] P. Liu, Y. Li, and Z. Zhang, "Circularly polarized 2 bit reconfigurable beam-steering antenna array," *IEEE Trans. Antennas Propag.*, vol. 68, no. 3, pp. 2416–2421, Mar. 2020.

[29] A. R. Weily and N. Nikolic, "Circularly polarized stacked patch antenna with perpendicular feed substrate," *IEEE Trans. Antennas Propag.*, vol. 61, no. 10, pp. 5274–5278, Oct. 2013.

[30] Y.-Q. Wen, B.-Z. Wang, and X. Ding, "Wide-beam circularly polarized microstrip magnetic-electric dipole antenna for wide-angle scanning phased array," *IEEE Antennas Wireless Propag. Lett.*, vol. 16, pp. 428–431, 2017.

[31] C. Y. Wei et al., "A dual circularly polarized SIW-fed phased array antenna with wide-angle beam scanning range," *IEEE Trans. Antennas Propag.*, vol. 70, no. 9, pp. 7393–7402, Sep. 2022.

[32] R. Behe and P. Brachat, "Compact duplexer-polarizer with semicircular waveguide (antenna feed)," *IEEE Trans. Antennas Propag.*, vol. 39, no. 8, pp. 1222–1224, Aug. 1991.

[33] T. Ege and P. McAndrew, "Analysis of stepped septum polarizers," *Electron. Lett.*, vol. 21, no. 24, pp. 1166–1168, Nov. 1985.

[34] J. Bornemann and V. A. Labay, "Ridge waveguide polarizer with finite and stepped-thickness septum," *IEEE Trans. Microw. Theory Techn.*, vol. 43, no. 8, pp. 1782–1787, Aug. 1995.

[35] J. D. Kraus and R. J. Marhefka, *Antennas For All Applications*. New York, NY, USA: McGraw-Hill, 2001.

[36] D. F. Kelley and W. L. Stutzman, "Array antenna pattern modeling methods that include mutual coupling effects," *IEEE Trans. Antennas Propag.*, vol. 41, no. 12, pp. 1625–1632, Dec. 1993.